



A new semi-solid casting technique for fabricating SiC-reinforced Mg alloys matrix composites



M. Esmaily^{a,*}, N. Mortazavi^b, J.E. Svensson^a, M. Halvarsson^b, M. Wessén^c,
L.G. Johansson^a, A.E.W. Jarfors^c

^a Department of Chemistry and Chemical Engineering, Chalmers University of Technology, SE-412 96 Gothenburg, Sweden

^b Department of Applied Physics, Chalmers University of Technology, SE-412 96 Gothenburg, Sweden

^c Department of Materials and Manufacturing - Casting, Jönköping University, SE-551 11 Jönköping, Sweden

ARTICLE INFO

Article history:

Received 24 October 2015

Received in revised form

23 January 2016

Accepted 10 February 2016

Available online 27 February 2016

Keywords:

A. Metal-matrix composites (MMCs)

B. Microstructures

E. Casting

Magnesium alloys

ABSTRACT

The capability of the newly developed rheocasting (RC) technique in combination with the RheoMetal process for producing SiC particulate-reinforced AM50 and AZ91D matrix composites (Mg-based MMCs) was investigated. The quality of the MMCs was studied by analyzing the fraction of casting pores, number density of SiC clusters and the uniformity of SiC particles. Solid fraction, particle size and oxidation of SiC particles had strong impacts on the overall quality of the MMCs. The MMCs produced by 40% solid fraction and oxidized micron-sized SiC particles exhibited an excellent casting quality. A low-quality MMC was obtained when non-oxidized sub-micron sized SiC particles were employed. The results showed the formation of various types intermetallic particles and carbides such as MgO, Mg₂Si, Al₂MgC₂, Mg₂C₃, Al₄C₃ as the interfacial reaction products of SiC/Mg alloy's melts. Mg hydride (α -MgH₂) was also identified in inter-dendritic regions of the MMCs for the first time.

© 2016 Published by Elsevier Ltd.

1. Introduction

Metal matrix composites (MMCs) are an emerging class of new materials that are being developed to improve the service performance of matrix metals and alloys. High-quality MMCs offer superior mechanical properties compared to their monolithic counterparts. They exhibit increased stiffness, tensile and fatigue strength, improved creep resistance and high temperature properties and increased wear resistance [1,2]. Magnesium (Mg) alloys combine high specific strength with good castability and excellent machinability and offer several advantages in relation to weight reduction and energy savings [3]. Combining the MMC technology with Mg alloys seems to provide the advantages of both MMCs and Mg alloys, and hence are known to be encouraging. MMCs based on Mg and Mg alloys matrices (Mg-MMC) are exceptional candidates for engineering lightweight structural materials, and are of great technological importance for many engineering applications, such as automotive and aerospace industries [4]. In general, Mg-MMCs are reinforced by various ceramic particles such as SiC, Al₂O₃,

Mg₂Si and carbon nanotubes; see for example [5–9]. They have been fabricated using a variety of methods such as stir casting [10], gas pressure infiltration [11], powder metallurgy [12,13], squeeze casting [14], spray deposition [15], injection molding [16] and in-situ techniques [17].

As an alternative to conventional casting methods, semi-solid metal (SSM) processing has shown the potential to produce Mg castings with a high level of complexity with a laminar flow of metal during mold filling [18]. This is the result of the higher viscosity of the semi-solid material, and reduces air entrapment compared to conventional casting methods, thereby produces castings with improved mechanical properties [19]. This paper deals with the microstructure of Mg-MMCs of two Mg alloys, namely alloy AM50 and AZ91D MMC produced through rheocasting (RC) technique which is a subcategory of SSM processing. RC is a casting process that offers cast components with very low pore content and high strength when a strict temperature control is achieved [20]. One promising method for preparing the slurries for the RC technique is the newly developed RheoMetal process, which is also known as the Rapid Slurry Formation (RSF) process [20,21]. The RheoMetal process converts a molten metal into slurry using internal enthalpy exchange between the liquid metal at relatively low superheat and a piece of solid metal attached to a stirrer. It has

* Corresponding author. Tel.: +46 317722864.

E-mail address: mohsen.esmaily@chalmers.se (M. Esmaily).

been shown that the RC method combined with the RheoMetal process has the potential to produce high quality AM50 and AZ91D Mg alloys with low casting defects [21,22] and that the environmental properties of Mg alloys can be notably mitigated by tailoring the microstructure through the component fabrication step using the RC technique.

The casting microstructure of Mg-MMCs is crucial to their performance in service. The main challenge may be to judiciously optimize the casting process to achieve uniformity and reproducibility provided that the host alloy and the reinforcement are suitable. Despite an abundance of research on Mg-MMC fabrication using conventional casting techniques, there very are few reports [23–26] dealing with the use of SSM processing, also known as “compocasting”, to produce this class of materials, and there are no published works on the use of RC and RheoMetal processes to fabricate Mg-MMCs. The objective of this investigation is therefore to document the influence of RC process on the microstructure of Mg alloy RC AM50-and AZ91D-based MMCs using two separated experiments. We first produced MMCs using non-oxidized nano-sized SiC particles, as a complex system, to analyze the formation of various types of intermetallic particles that may form during solidification in SiC-reinforced Mg alloys. In the second experiment, we examined the capabilities of RC process in producing sound Mg alloys-based MMCs using two different solid fractions through quantitative assessments of the MMCs’ microstructures. Thus, the uniformity of SiC particles, casting defects and microstructure of the host alloys were characterized using image analysis techniques.

2. Experimentation

2.1. Fabrication of SiC-reinforced MMCs

The RC AM50, AZ91 and Mg-MMCs were produced using the RC process, see the schematic illustration of the casting procedure in Fig. 1. The casting machine was manufactured by Suzhou Sanji Foundry Co Ltd. The machine had a locking force of 50 tonnes. The die had a projected area of 250 cm², making it possible to produce cast components having wall thicknesses of 7, 12 and 20 mm. The slurry for the RC process was prepared using the RheoMetal process, where a molten metal is converted into slurry using internal enthalpy exchange material (EEM) between the liquid metal at relatively low superheat and a piece of solid metal attached to a stirrer. The EEM was cast onto a steel rod. The rod was then immersed into the melt while stirring after it had been cooled down to a moderate temperature. During this process, the melt was cooled down rather quickly during the melting of the EEM, and at the end, homogeneous slurry was prepared. An advantage of the RheoMetal process has already been discussed in Refs. [20–22,27–29]. In this way, the solid fraction (f_s) can be easily controlled in a robust way by the initial temperatures of the melt and the EEM as well as the EEM to melt ratio. Control of the f_s was necessary to be able to meet the requirement that the slurry be pourable into the shot sleeve of a die casting machine.

Commercial Mg alloys AZ91D and AM50 alloys were used as the matrices. Their chemical compositions were analyzed through

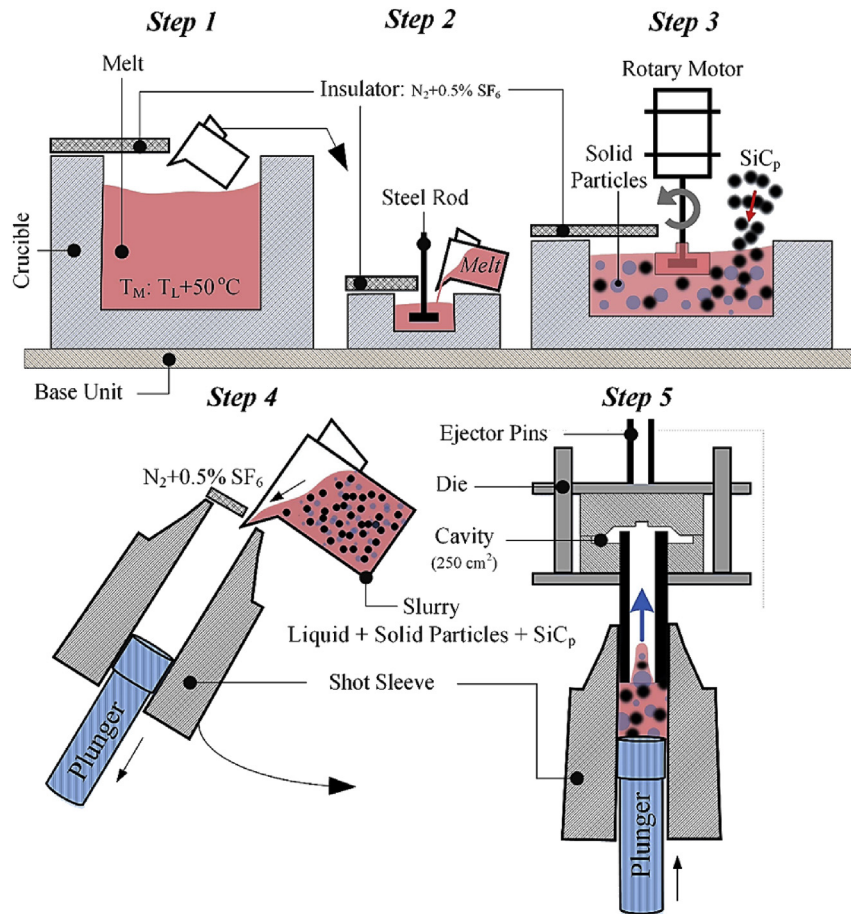


Fig. 1. Schematic of the RC process used for preparing the RC alloys and Mg alloys-MMCs; step 1: melt preparation, step 2: EEM preparation, step 3: rheo-processing (slurry preparation) (SiC particulates were added into the melt at this stage for fabricating the MMCs), step 4: pouring the slurry into the shot sleeve, and step 5: high pressure casting unit. Note: Step 1 and 3 were performed in the same furnace but with some time intervals.

Table 1
Chemical composition (wt. %) of the alloys investigated.

Material	Mg	Al	Zn	Mn	Si	Fe	Cu	Ni
RC AZ91D	Bal.	8.9	0.74	0.21	0.008	0.0022	0.0007	0.0004
RC AM50	Bal.	5.0	0.01	0.25	0.01	0.0016	0.001	0.0007

optical mass spectroscopy and are listed in Table 1. In the present investigation, the MMCs were produced using two different SiC particle sizes and two different f_s values. Two different procedures that were employed for making the composites are described in Table 2. In the first experiment, Mg alloy AM50 and AZ91D were reinforced with SiC particles in the size range 0.1–1.9 μm (with the commercial name: HCS 59N) using an f_s of 60%. In the second experiment, Mg alloy AZ91D was reinforced with bigger SiC particles in the size range 4–28 μm (with the commercial name: HCS 400) at two f_s values of 30 and 60%. In addition, we oxidized the larger SiC particles prior to casting at 1100 °C for 45 min. In both sets of experiments, Mg alloy matrix composites were reinforced with 10 vol.% of high purity SiC particles. More details regarding the process parameters, including the stirring time, stirring speed, and protection of the slurry, are listed in Table 2.

2.2. Material characterization techniques

As-cast materials were cut into cross-sections of the RC AM50 and AZ91D as well as the Mg alloys-based MMCs with an area of about 4.2 mm² for microstructural characterization. The sectioned samples were mounted in cold-setting epoxy resin. The mounted samples were then ground, lubricated with de-ionized water, with successive grades of silicon carbide abrasive papers (SiC grit papers) from P800 to P4000 mesh. Polishing was then performed using cloth discs and diamond paste in sizes ranging from 3 to 1 μm , followed by a fine polishing step using OPS colloidal silica (0.25 μm) for 120 s on a Buehler Microcloth. The specimens were cleaned with distilled water, degreased with acetone, washed again with distilled water, and dried by cool air with a blower. They were then stored in a desiccator before and during examinations. Considering the difficulties associated with the microstructural quantification in the cast Mg–Al alloys, both polished and etched samples were investigated. A solution of Nital (5 ml HNO₃ + 95 ml ethanol) was used as the etchant to reveal the microstructure. An Olympus GX-71 optical microscope (OM) and a FEI Quanta 200 environmental scanning electron microscope (ESEM) equipped with energy dispersive x-ray (EDX) micro-analysis hardware were used for imaging. The instrument comes equipped with an Oxford Inca EDX with a Silicon Drift Detector (SDD) (Beryllium window). The EDX analysis was carried out using 15 kV accelerating voltage. The grain size measurements were carried out based on the Feret diameter

Table 2
Details of the RC process used in this study for fabricating the MMCs.

Process steps	A (HCS 59N)	B (HCS 400)
Particle size	0.1–1.9 μm	4–28 μm
Added amount of SiC _p	10%	10%
Oxidation treatment	N/A	1100 °C 45 min in air
SiC _p addition temperature	25 °C	>850 °C
Melt holding temperature	T _L +50 °C	T _L +50 °C
Protection	N ₂ + 0.5% SF ₆	N ₂ +0.5% SF ₆
Stirring speed	Varying 500–800 rpm	Varying 500–800 rpm
EEM	Particle free	Particle free
EEM temp	100–120 °C	100–120 °C
EEM amount	5%	4, 5%
Corresponding amount solid	60%	40, 60%
Stirring time	45 min	45 min

that is defined as the distance between two parallel tangential lines rather than planes [30]. The aspect ratio of grains in the materials was calculated using $F = 4 \pi A/P^2$, where A is the area and P is the peripheral length of a grain.

Quantitative characterization was performed using statistical analyses in order to examine the grain size and fraction of casting pores. Different types of software, namely Adobe Photoshop CS4, Image Pro-Plus and ImageJR were used for scrutinizing micrographs. The uniformity of SiC particulates was investigated using the nearest neighbor distance (NND) distribution function and the quadrat method. The NND function was used to describe the arrangement of SiC clusters ($\geq 40 \mu\text{m}$) in a quantitative manner. The NND is a probability density function such that $P(r) dr$ is the probability of finding the nearest neighbor of a particle with the same characteristics in the distance range r to $(r + dr)$; see Refs. [22,31] for more details. The quadrat method was chosen to study the distribution of SiC particles, see Refs. [32,33]. The quadrat method was used for the samples containing bigger SiC particles and much less clustering. To do this, the SEM micrographs were divided into square cells and the number of SiC particulates in each quadrat, N_q , was counted. In general, an ordered particle distribution would be expected to generate a large number of quadrats containing approximately the same number of particles. On the other hand, a clustered distribution would be expected to produce a combination of empty quadrats, quadrats with a small number of particles, and quadrats with many particles. A random distribution would be expected to produce results somewhere in between these two extremes. In this study, the quadrat method was carried out on 25 micrographs within square fields, 600 \times 600 pixels in size. Each field was divided into 225 contiguous quadrats. A quadrat size of 40 \times 40 pixels was selected. The calculated particles number per cell distributions were then compared to the two theoretical distributions; (a) the Poisson distribution (Equation (1)) and (b) the negative binomial distribution (Equation (2)) according to the followings [33];

$$P(r) = \frac{\mu^n}{r!} \exp(-\mu) \quad (1)$$

$$P(r) = \left(\frac{(k+r-1)!}{(k-1)!r!} \right) \left(\frac{p}{1+p} \right)^r \left(\frac{1}{1+p} \right)^k \quad (2)$$

where $P(r)$ indicates the probability, r denotes the number of particles per cell, μ is the mean value of the number of particles per cell, and k and p are parameters that can be determined according to [32]. According to the above two types of distribution, the Poisson distribution corresponds to a homogenous particle distribution and the negative binomial distribution corresponds to a clustered type of particles distribution. To examine the effect of oxidation on the composition of the surface film formed on SiC particles high-resolution Auger electron spectroscopy (HR-AES) was employed. Analysis was performed in a site-specific manner on large SiC particles. The analyses were conducted using a Physical Electronics Model 700 Scanning Auger Nanoprobe (LS) apparatus equipped with a spherical sector analyser. Spectra were recorded in direct mode and with a 2–5 keV and 1 nA primary beam.

Transmission Electron Microscopy (TEM) was employed to shed light on the microstructure of Mg alloy AZ91D-based MMC using a Titan 80–300 TEM/STEM instrument operating at 300 kV. The microscope was equipped with an Oxford Inca EDX detector. An FEI Versa 3D combined Focused Ion Beam/Scanning Electron Microscope (FIB/SEM) workstation was used to create and investigate cross-sections of the oxide scales and subjacent metal of the exposed samples. The thin lamella was mounted on a support Cu-

grid. Time-resolved low-loss electron energy loss spectroscopy (EELS) was performed on FIB-prepared TEM thin foils of the Mg-based MMCs using a monochromated and aberration-corrected transmission electron microscope at 80 kV. Finally, micro-Vickers hardness was measured (Akashi HV-114) on the polished surfaces of the samples. The mean values of 20 measurements were obtained under the condition of a 0.1 kgf load with a duration of 15 s.

3. Results

3.1. RC AZ91D and AM50 microstructures

The microstructural constituents of the cast Mg–Al alloys, especially AM50 and AZ91D, have been widely studied by numerous authors; see for example [34–36]. The main microstructural constituents are α -Mg grains surrounded by interdendritic regions (also called eutectic α) and β phase particles ($\text{Mg}_{17}\text{Al}_{12}$). Owing to the presence of Mn, Mg–Al alloys in the AM and AZ series also contain a small amount of η phase particles ($\text{Al}_8\text{Mn}_5\text{Fe}_x$) [22,28,29]. Moreover, transient phases such as Mg_5Al have been reported in the microstructure of Mg–Al alloys [28]. This is a precursor of β - $\text{Mg}_{17}\text{Al}_{12}$ and has considerably lower volume fraction than the dominant intermetallic phase particles. Fig. 2 shows SEM micrographs of the microstructure of RC Mg alloys AM50 and AZ91D. SEM/EDX of the main microstructural constituents in the RC materials are provided in Table 3. Both microstructures consisted of externally solidified dendritic grains (ESGs) and finer grains designated internally solidified grains (ISGs). The ESGs are large grains that are usually formed prior to the melt entering

Table 3

Typical composition of the main phases (at.%) from the points designated in Fig. 2.

Point	Probable phase	Mg	Al	Mn	Zn	Fe
1 (AM50)	α -Mg	98.2	1.8	–	–	–
2 (AM50)	β phase ($\text{Mg}_{17}\text{Al}_{12}$)	62.5	37.5	–	–	–
3 (AM50)	η phase ($\text{Al}_8\text{Mn}_5(\text{Fe})$)	24.1	47.5	27.8	–	0.4
4 (AZ91D)	α -Mg	97.1	2.9	–	–	–
5 (AZ91D)	β phase ($\text{Mg}_{17}(\text{Al}, \text{Zn})_{12}$)	60.5	36.4	–	2.1	–
6 (AZ91D)	η phase ($\text{Al}_8\text{Mn}_5(\text{Fe})$)	3.9	47.1	48.9	–	0.1

the casting and in the shot-sleeves. However, ESGs can also be fragmented during their passage through the gating system [22].

In both cases, the β phase component appeared in the interdendritic regions. As expected, a comparison of the microstructures produced by RC AM50 and AZ91 showed that the β phase tended to form relatively fine particles in RC AM50 while the β phase particles in the RC AZ91D alloy were coarser and more continuous and appeared with a higher area fraction. The average α -Mg grain sizes of RC AM50 and RC AZ91D were calculated to be ~45 and 25 μm , respectively. Using electron backscattered diffraction (EBSD) technique, we have previously shown that the RC process produces a semi-dendritic grain structure with a higher aspect ratio compared to those produced by conventional high pressure die-casting (HPDC) [22]. The aspect ratio of α -Mg grains in the alloy matrices was calculated to be 0.69 and 0.72 for the RC AM50 and AZ91D, respectively.

Table 3 represents the EDX point analyses performed at six positions in the microstructure of RC AM50 (points 1, 2 and 3) and AZ91D (points 4, 5 and 6) designated in Fig. 2. The center of the α -

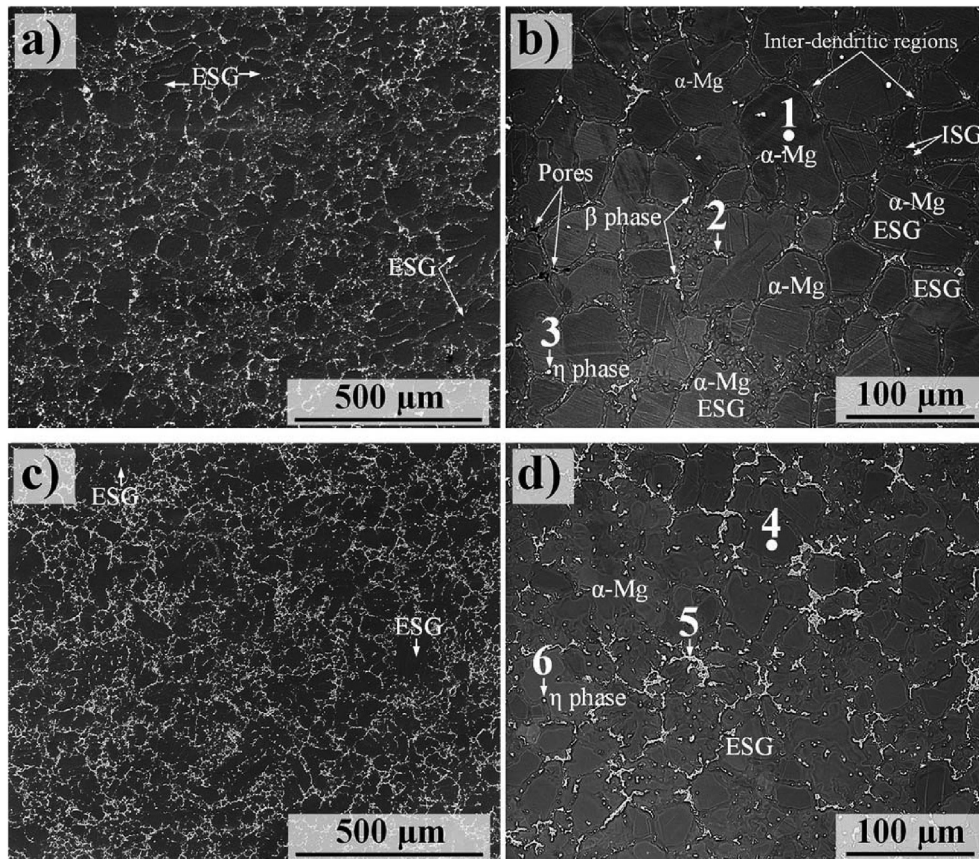


Fig. 2. SEM micrographs showing typical microstructures of alloys; (a) and (b) AM50, (c) and (d) AZ91D produced by RC techniques. EDX point analysis of 1, 2, 3, 4, 5 and 6 is listed in Table 3.

Mg grains contained ~1.8 and 2.9 at.% Al in RC AM50 and AZ91D, respectively; see P1 and P4. The EDX analysis showed that the β phase particles in both RC and HPDC AM50 exhibited an Al concentrations somewhat lower than the eutectic composition, see the binary Mg–Al phase diagram [37,38]. The detection of less Al content in β particles in Mg–Al alloys by SEM/EDX stems from the fact that the EDX detector is normally affected by the surrounding matrix [22]. Thus, detect more Mg and less Al content is usually expected when analyzing the intermetallic particles by EDX. In addition, the EDX analyses revealed the presence of small amount of Zn in the β phase intermetallic compounds, presumably through replacement of Al atoms. The brightest particles (designated as P3 and P6 in Table 3) in the SEM images (Fig. 2b and d), were η phase particles that mainly contain Al and Mn. It may be noted that Fe was present in the η intermetallic particles. Hence, the solidification microstructure of the fabricated RC AM50 and AZ91D also contained $Al_8(Mn_{5-x}Fe_x)$ intermetallic particles in which Fe replaced some of the Mn atoms.

3.2. SiC-reinforced AM50 and AZ91D microstructures

Fig. 3 depicts the morphology and size distribution of the two types of SiC particles used to fabricate the Mg alloys-based MMCs. The particle size distribution (PSD) of the particles was determined through image analysis on high-magnification SEM micrographs. It was clear that there was a huge difference in the size of the two types of particles used in this study.

In the case of HCS 59N, PSD analyses revealed that 85% of the particles are in the range 0.4–1.2 μm with an average particle size of about 0.7 μm . A low percentage of particles (~2.2%) was in the nanometer range, showing an average size of less than 100 nm. In the case of the SiC particle type HCS 400, particles exhibited an average size of about 13.1 μm , approximately 19 times bigger than the type HCS 59N. Besides, there were some fractions of particles having an average size in the range 25–40 μm .

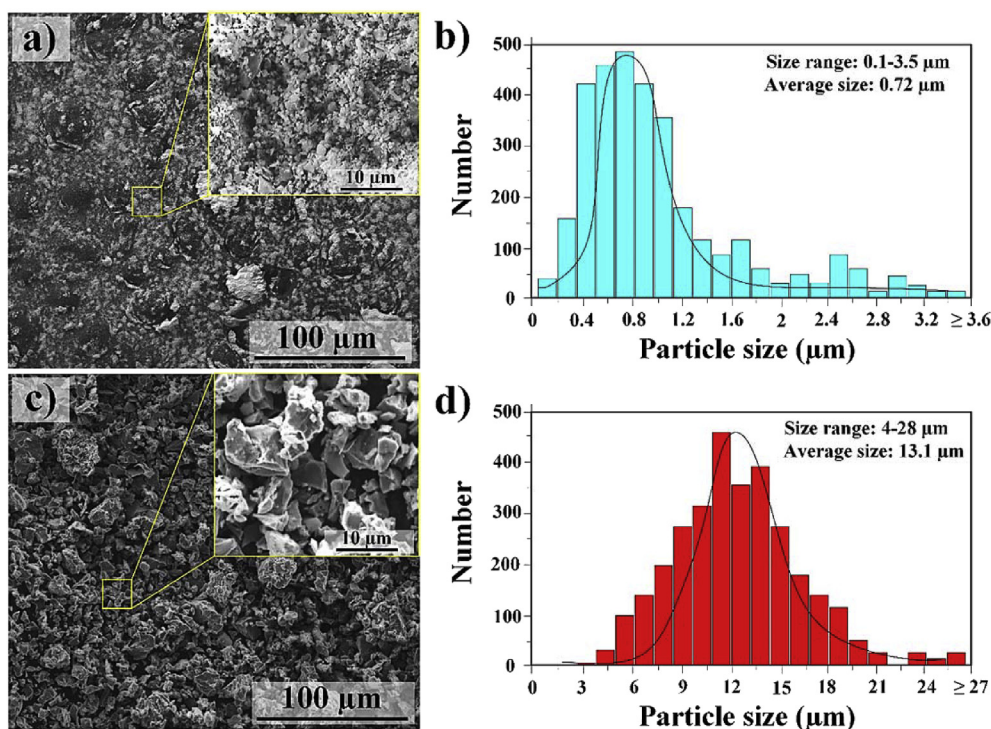


Fig. 3. SEM micrographs and particles size distribution of SiC particles used to produce the Mg-MMCs; (a) and (b) HCS 59N, (c) and (d) HCS 400.

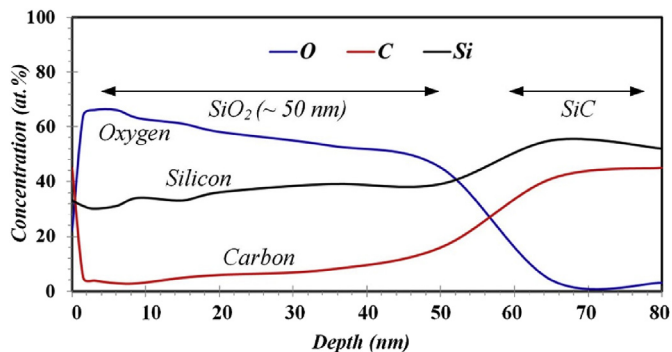


Fig. 4. AES depth profile showing the formation of silica (SiO_2) on the SiC particles upon their oxidation at 1100 $^{\circ}\text{C}$ for 45 min.

It has been reported that heating SiC particles up to 900 $^{\circ}\text{C}$, not only helps elimination of surface impurities and in the desorption of gases, but also changes the surface composition by forming an oxide layer on the surface [39]. Fig. 4 shows an AES depth profile acquired from the surface of large oxidized SiC particle type HCS 400 artificially oxidized at 1100 $^{\circ}\text{C}$. Three AES analyses were conducted on particles larger than 5 μm in order to determine the thickness of the oxide layer formed on SiC particles. From the profile, the outmost layer of the analyzed particles contained high concentration of C. This layer was observed in all three particles and is attributed to surface contamination. Below this layer, silica (SiO_2) was present. The thickness of this layer was found to vary 30–50 nm from one particle to another, probably in relation to the particle surface exposed to electron beam. Such variations in the oxide layer thickness have also been reported in other studies, where this behavior is explained by the fact that oxidation is strongly governed by the surface exposed to O, being faster for the C

face than for the Si face [39,40]. As indicated above, the oxidized particles were employed in the second experiment.

3.2.1. The first experiment-non-oxidized HCS 59N SiC particles

Fig. 5 shows the microstructure of the Mg alloy AM50 and AZ91D reinforced by SiC particles type HCS 59N using the RC method. These alloys were produced using an f_s of 60%. In this experiment, SiC particles were not oxidized and just pre-heated to 50 °C for drying. As seen in the SEM images, in both AM50- and AZ91D-based MMCs, SiC clusters could frequently be observed. Quantitative data on the quality of the alloys and MMCs and the particles' uniformity are provided below.

In the case of alloy AM50-based MMC (Fig. 5a and b), morphological inspections revealed that the addition of SiC particles introduced some changes in the grain structure of the alloys. Firstly, a notable reduction in the average α -Mg grain size, reaching a value of about 28 μm , was observed in alloy AM50-based MMC. This can be compared to the average α -Mg grain size in the RC AM50, compare Fig. 5b with Fig. 2b. Secondly, SiC additions gave rise to an increase in the aspect ratio of α -Mg grains, showing an aspect ratio of ~ 0.8 , signifying an increase in the sphericity of primary α -Mg. Notably, very little evidence of β phase particles in the interdendritic regions was observed (see Fig. 5a and b). The β phase particles were substituted with a new phase containing some percentages of Si and C in addition to Mg and Al (see point 3 in Fig. 5b and Table 4). Similar observations were made in the case of alloy AZ91D-based MMC (Fig. 5c and d). Thus, a comparison between the RC AZ91 and RC AZ91-based MMC showed that the size of α -Mg grains decreased from 25 μm to 21.4 and the aspect ratio

Table 4

Typical composition of the main phases (at.%) from the points designated in Fig. 5.

Point	Probable phase	Mg	Al	C	Si	Zn
1 (AM50)	α -Mg	97.2	1.7	1.1	–	–
2 (AM50)	$\sim \text{Al}_2\text{MgC}_2$	23.7	35.3	41	–	–
3 (AM50)	–	75.5	17.8	1.9	4.8	–
4 (AM50)	SiC particle	1.5	0.5	44.3	53.7	–
5 (AZ91D)	α -Mg	95.65	2.75	1.6	–	–
6 (AZ91D)	β phase ($\text{Mg}_{17}(\text{Al}, \text{Zn})_{12}$)	59.7	37.6	1.2	–	1.5

also increased from 0.72 to 0.79, respectively. Similar to RC AM50-based MMC, some fractions of β phase particles in the RC AZ91D-based MMC (see the dark regions in the surrounding areas of β phase particles in Fig. 5c) were replaced with a phase containing Si, C, Mg and Al. Otherwise, β phase formed in the RC AZ91D-based MMC showed a composition almost similar to its original chemical composition with some addition of C; compare point 6 in Table 4 with point 5 in Table 3.

Table 4 lists the EDX analyses at the six points in the microstructure of RC AM50- (points 1, 2, 3 and 4) and AZ91D-based MMCs (points 5 and 6) designated in Fig. 5. In both cases, α -Mg grains (points 1 and 5) contained 1–2 at.% C content, which is likely related to surface contaminations introduced to the sample's surface during the grinding/polishing step. Point 2 in Fig. 4a revealed a chemical composition very close to Al_2MgC_2 carbide, appearing as almost spherical particles in the MMCs' microstructures. This carbide, which was chemically analyzed through EDX and high resolution SEM, could not be detected by XRD due to its small fraction. The phase was previously communicated as one of the most

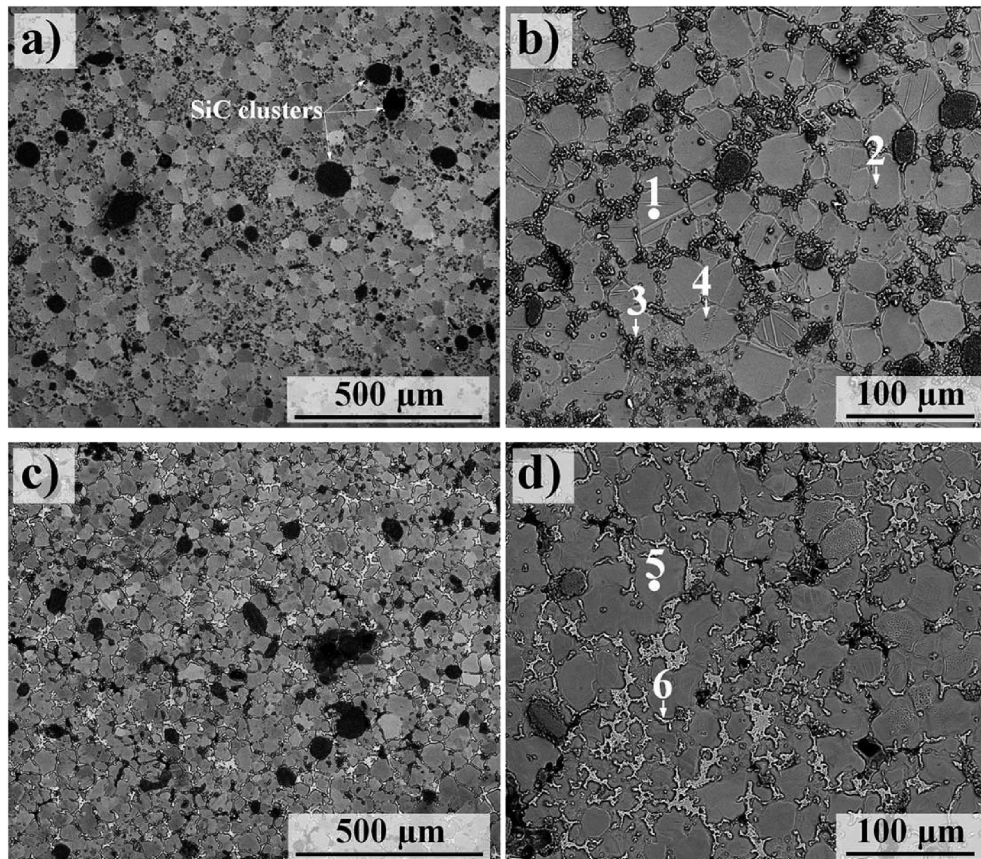


Fig. 5. SEM micrographs showing the microstructure of Mg-based MMC (HCS 59N) produced through the RC method; (a) and (b) alloy AM50-based MMC, (c) and (d) alloy AZ91D-based MMC. Note: the f_s of slurry for these experiment was 60%. EDX point analysis of 1, 2, 3, 4, 5 and 6 is listed in Table 4.

probable carbides in Mg-based MMCs [41–44]; see the XRD diffractograms below. Notably, it was noticed that some SiC particles (point 4 in Fig. 5b and Table 4) had been trapped within α -Mg grains almost in the center of ECSs, presumably between dendrite side arms.

3.2.2. The second experiment-oxidized HCS 400 SiC particles

In this part of the study, alloy AZ91 was reinforced using the oxidized SiC particle type HCS 400. Fig. 6 shows the as-cast microstructure of alloy AZ91-based MMC produced by HCS 400 using two f_s values of 40 (Fig. 6a and b) and 60% (Fig. 6c and d). An overall inspections showed that while the sub-micron SiC particles were distributed almost at everywhere including inter-dendritic regions and also in the interior of α -Mg grains in the MMC produced in the first experiment, the micro-sized SiC particles were mostly distributed in the inter-dendritic regions. SiC particulates and clusters were recognizable in SEM images. Clustering of SiC particles was much less pronounced when using HCS 400 compared to those containing SiC particle type HCS 59N (compare Figs. 5 and 6). Furthermore, SiC clustering was considerably minimized when f_s was 40%; compare Fig. 6a and b with Fig. 6c and d. This was also supported by the statistical analyses; see below. Grain size measurements showed that the use of particle type HCS 400 resulted in an average α -Mg grain size of ~23 and 21 μm for the f_s values of 40 and 60%, respectively. Thus, a coarser grain structure in alloy AZ91D was formed with the same fraction of solids (60%) when using particle type HCS 400 rather than HCS 59N; compare Fig. 6a and b with Fig. 5c and d.

The SEM/EDX analyses of some of the microstructural features, i.e. points 1, 2 and 3, are provided in Table 5. The number of

Table 5

Typical composition of the main phases (at.%) from the points designated in Fig. 6.

Point	Probable phase	Mg	Al	C	O	Zn
1	α -Mg	97.2	2.6	0.2	–	–
2	β phase ($\text{Mg}_{17}(\text{Al}, \text{Zn})_{12}$)	60.5	36.5	0.1	–	2.9
3	Mg_2C_3	42.1	–	57.9	–	–

intermetallic particle types could be identified by SEM/EDX was much less in the microstructure of composites produced in the second experiment compared to the first experiment (see also below). The C content of the β phase particles was considerably decreased. Thus, β phase intermetallic particles exhibited a chemical composition very close to those formed on RC AZ91D; compare point 2 in Table 5 with point 5 in Table 4. In addition to SiC particles and the main constituents, there was evidence for a type of Mg carbide, Mg_2C_3 ; see point 3 in Table 5. These carbide had a band-like morphology and were formed adjacent to the SiC particles. It was noted that the fraction of Mg_2C_3 increased with increasing f_s . This could be attributed to the more mechanical contact between the EEM and the SiC particles-containing melt during the slurry preparation. It may be noted that the formation of this carbide has also been reported in Refs. [42,43].

3.3. Phase identification using XRD, TEM/EDX and EELS

Fig. 7 displays XRD patterns (a grazing incidence angle of 0.5°) of the RC AM50- and AZ91-based MMCs (HCS 59N). In both cases, relatively low intensity peaks corresponding to the β phase ($\text{Mg}_{17}\text{Al}_{12}$) were present in addition to the peaks corresponding to

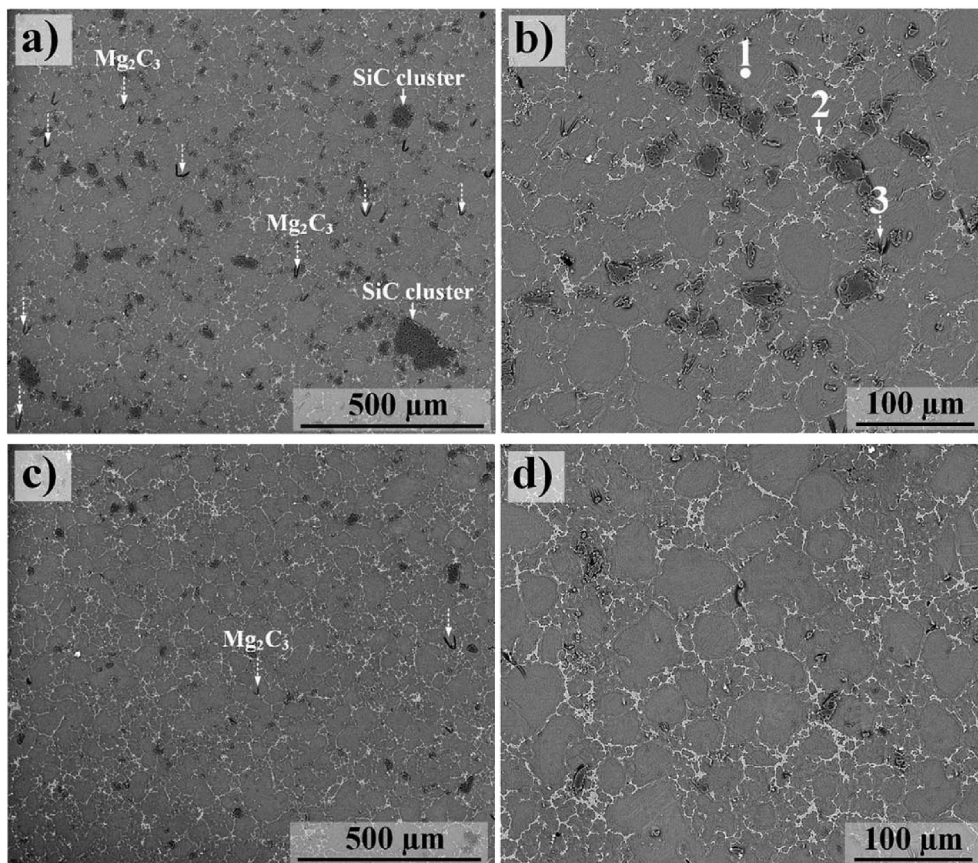


Fig. 6. SEM micrographs showing the cast microstructure of alloy AZ91D-based MMC produced using SiC particle type HCS 400 produced by the RC method; (a) and (b) $f_s = 60\%$, (c) and (d) $f_s = 40\%$. EDX point analysis of 1, 2, 3, 4 and 5 is listed in Table 5.

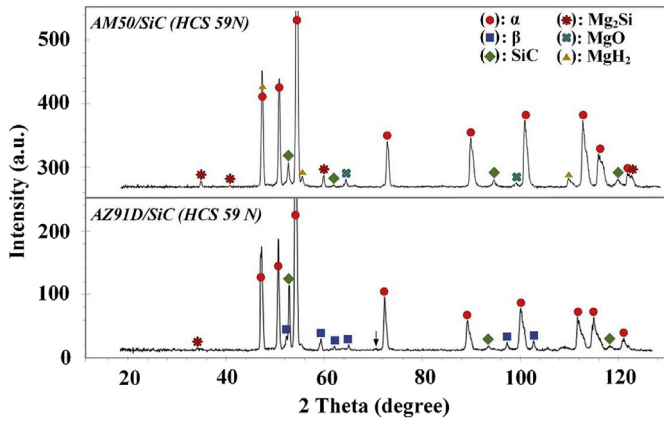


Fig. 7. XRD diffractograms (obtained by an incidence angle of 0.5°) collected from the RC AM50- and AZ91D reinforced by SiC particle type HCS 59N using the slurry with an f_s of 60%. Note: the peak shown by arrow for the case of Mg alloy AZ91D-based MMC could not be attributed to any unknown crystalline compound.

α -Mg. While the peaks related to β phase appeared with higher intensity and could be easily detected for the case of alloy AZ91D, they were hardly recognizable in the case of alloy AM50, which is in line with microstructural inspections (see Fig. 5). The XRD analysis showed no evidence of the AlMn phase, which is likely due to their low volume fraction. In both cases, strong peaks related to β -SiC were obvious. Peaks corresponding to Mg_2Si intermetallic particles and MgO had a higher intensity for the alloy AM50 than AZ91D. Surprisingly, some peaks had characteristics very similar to Mg hydride (MgH_2) in both MMCs.

In all the XRD analyses performed, there was no indication of carbides in the XRD analyses using grazing incidence angle of 0.5° , which is consistent with the XRD patterns of SiC reinforced Mg-based MMCs. XRD patterns related to the MMCs (HCS 400) were not shown as the only phases that could be detected in those cases were the main phase, i.e. α -Mg, β phase and SiC particles.

TEM analysis was performed to further elucidate the effect of SiC additions on the formation of different phases. From qualitative SEM imaging (see the SEM images in Figs. 5 and 6), it was obvious that SiC particles tended to accumulate in the inter-dendritic regions. Fig. 8 shows the STEM/EDX and STEM/EELS investigations performed on a FIB-prepared thin foil from an inter-dendritic region of Mg alloy AZ91D reinforced by SiC particle type HCS 59N. The darker area (point A in Fig. 8a and Table 6) confirmed an Al content of 7.9 at.% indicating that the studied area was an inter-dendritic region. As seen, an island (the brighter area in Fig. 7a) was formed inside the inter-dendritic region. Point B in Table 6 shows the chemical composition of this island, where a composition similar to point A was detected with some additions of Zn. The bright particles in Fig. 8a were SiC particles; see the chemical composition of C in Table 6. Note that the C content of the SiC particles was less than their stoichiometric composition. MgO and Mg_2Si were also present close to SiC particles; see for e.g. points E and D in Fig. 8a and b and in Table 6. We also found another carbide consisted of Al and C, showing the chemical composition of Al_4C_3 (point E).

Fig. 8c provides the time resolved and normalized EELS spectrum of the point designated by a cross in Fig. 8b, adjacent to the SiC particle. The EELS analysis indicated the presence of MgH_2 in the alloy's microstructure, which is in line with the detection of MgH_2 by XRD (Fig. 7). Thus, at time 0s, two volume plasmon peaks of

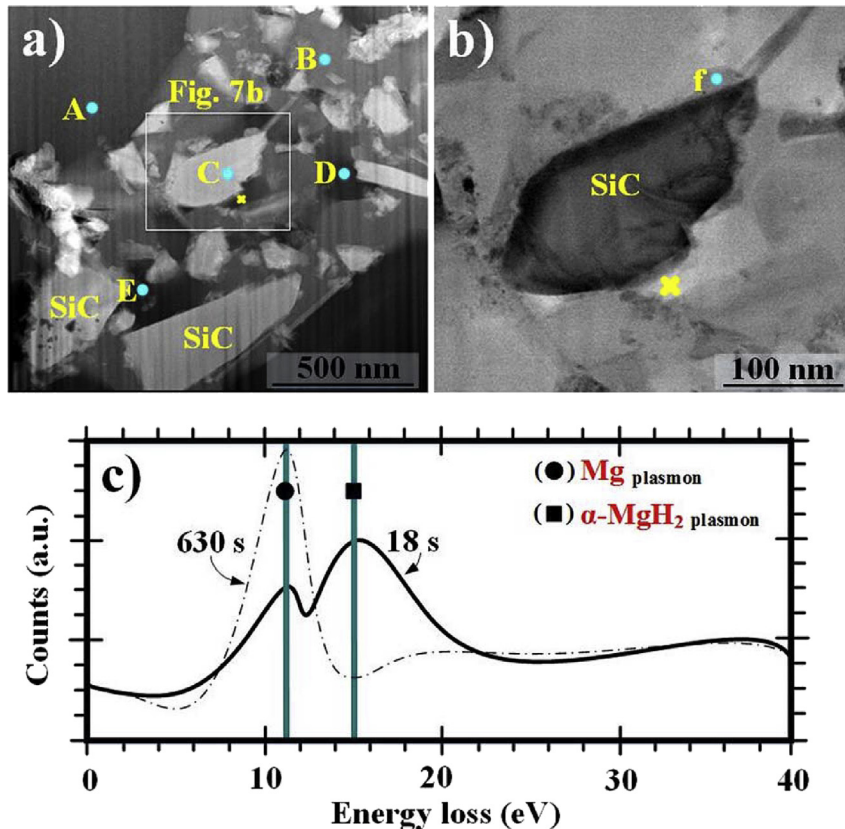


Fig. 8. STEM investigation on inter-dendritic regions of Mg alloy AZ91D reinforced by SiC particle type HCS 59N; (a) high-angle annular dark-field (HAADF) STEM micrograph, (b) bright-field STEM micrograph and (c) EELS spectra of the point designated by a cross in Fig. 8a and b. TEM/EDX point analysis A, B, C, D and E are presented in Table 6.

Table 6
TEM/EDX Chemical compositional analyses (at.%) from the points designated in Fig. 8.

Point	Probable phase	Mg	Al	C	Si	Zn	O
A	Inter-dendritic region	89.6 ± 1.2	7.9 ± 1.1	2.5 ± 0.3	–	–	–
B	Inter-dendritic region	86.7 ± 0.8	8.1 ± 0.4	3.3 ± 0.1	–	1.9 ± 0.1	–
C	SiC particles	–	–	41.9 ± 1.4	58.9 ± 2	–	–
D	MgO	51.7 ± 2.3	0.1 ± 0.01	0.2 ± 0.02	–	–	48 ± 1.1
E	Al ₄ C ₃	0.9 ± 0.3	54.5 ± 0.2	44.6 ± 3.2	–	–	–
f	Mg ₂ Si	63.55 ± 0.5	0.15 ± 0.01	2.3 ± 0.03	34 ± 1.9	–	–

~10.6 and 14.55 eV were acquired corresponding to the Mg and α -MgH₂, respectively [45,46]. The relative intensity of the Mg peak increased as the exposure time to the electron beam increased, and after 630 s the peak corresponding to α -MgH₂ had vanished and the phase was transformed into Mg due to the hydrogen loss from the hydride particle.

3.4. Materials quality; quantitative analyses

The uniformity of SiC particles and clusters as well as the fraction of casting defects were investigated in order to examine the MMCs' quality. It should be noted that statistical analyses can provide broader, and thus more precise, descriptions of the MMCs' quality as they were determined from a relatively large area (4.2 mm²). The NND of SiC clusters larger than 40 μ m, approximately equal to twice the size of the largest SiC particulates employed in this study, for alloy AZ91D reinforced by the two particle types and at the two different f_s values are presented in Fig. 9a. From the statistical data, it was clear that the number of clusters in the studied areas was in the order of HCS 59N ($f_s = 60\%$) >> oxidized HCS 400 ($f_s = 60\%$) > oxidized HCS 400 ($f_s = 40\%$); see the x-axis in Fig. 9a. Thus, while the clustering was most probable when employing the particle type HCS 59N, it was markedly

minimized when using the oxidized particle type HCS 400 with a lower f_s , which was in accordance with the qualitative assessments; see above.

In addition, the NND results indicated a large number SiC clusters were present at a lower distance interval (90–180 μ m) and a small number clusters at the high distance intervals (more than 180 μ m) in the microstructure of alloy AZ91D reinforced by the SiC particle type HCS 59N in comparison with those reinforced by the oxidized particle type HCS 400 at the two f_s values of 40 and 60%. Moreover, it was evident that at $f_s = 40\%$ less clustering of the SiC particles occurred. Therefore, in that case SiC clusters were more frequently formed at very high distance intervals (≥ 240 μ m). It should be mentioned that the NND analysis of the RC alloy AM50 reinforced by HCS 59N (Fig. 5a and b) showed a somewhat similar pattern to the alloy AZ91D reinforced by the same particle type. The results obtained from the quadrat method (Fig. 9b and c) provided a general picture of the distribution of SiC particles owing the large area fraction of the investigation. Quadrat analysis was performed only on MMCs exhibiting much less SiC clustering and hence relatively better casting quality, i.e. Mg alloy AZ91D reinforced by oxidized particles type HCS 400 at the two f_s values. The number of SiC particles per quadrat was meaningfully different between MMCs produced by the two fractions of solid (Fig. 9a and b). Thus,

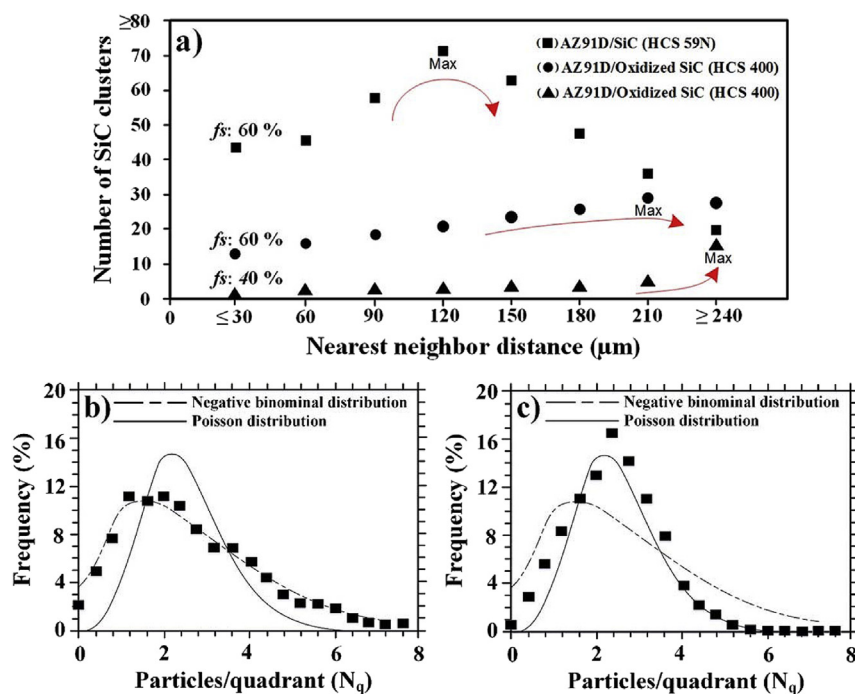


Fig. 9. Clustering analysis: quantitative analyses of the MMCs' quality fabricated by the RC process; (a) the NND of SiC cluster larger than 40 μ m. Particle distribution analysis: typical distributions of SiC particles per quadrat N_q for alloy AZ91D reinforced by the oxidized SiC particle type HCS 400 with an f_s value of (b) 60% and (c) 40%. Note: the statistical data presented in each figure were determined using 25 SEM images taken from relatively large areas (~4.2 mm²) of the MMCs' microstructures.

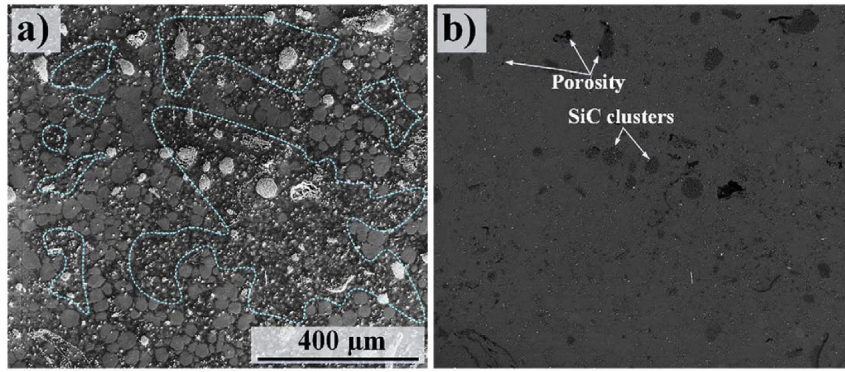


Fig. 10. (a) Secondary electron (SE) and (b) backscattered electron (BSE) SEM micrographs showing the same area, 2 mm from the casting skin, in the RC alloy AM50 reinforced by the SiC particle type HCS 59N. Note: the area separated by dotted-lines in Fig. 10a shows the regions containing grains with smaller size.

the Mg alloy-based MMC produced using an f_s of 60% followed the negative binomial distribution, whereas the MMC produced using an f_s of 40% followed the Poisson distribution type, confirming the uniform distribution of SiC particles in the latter case.

The SEM micrographs shown above (Figs. 2, 5 and 6) were taken from the central regions of the castings. Inspecting areas close to the castings' skins also resulted in some information on the materials' microstructure and casting defects. Fig. 10 shows an area ~1 mm from the cast skin in alloy AM50-based MMC. This micrographs shows the poorest part of the MMC, from a quality point of view. As expected [22], the grain structure became finer when approaching the cast skin. Frequently, regions exhibiting considerably fine α -Mg grains in the range 1–4 μ m could be observed; see these regions in Fig. 10a. Similar regions could also be seen in the central regions of the castings, but to a lesser extent. Besides,

particle-porosity association could be often observed, see the worst regions (from porosity point of view) in Fig. 10. Such regions consisting of grain with extremely non-uniform size and SiC-associated defects were also present in the case of RC alloy AZ91D reinforced by the particle type HSC 59N, but could not be seen in the MMCs produced by the particle type HCS 400. To have a broader image of the extent of casting defects, the fraction of casting defects were determined.

Fig. 11 shows the morphology of pores and the quantitative assessments of the porosities in the materials produced by the RC technique. The SEM image in Fig. 11a shows relatively large connected casting pores in the MMC produced by HCS 59N. In the case of the MMC (HCS 400), the pores were significantly smaller and were only formed in the inter-dendritic regions; see Fig. 11b. The data shown in Fig. 11c were obtained from an area of 4.2 mm² and

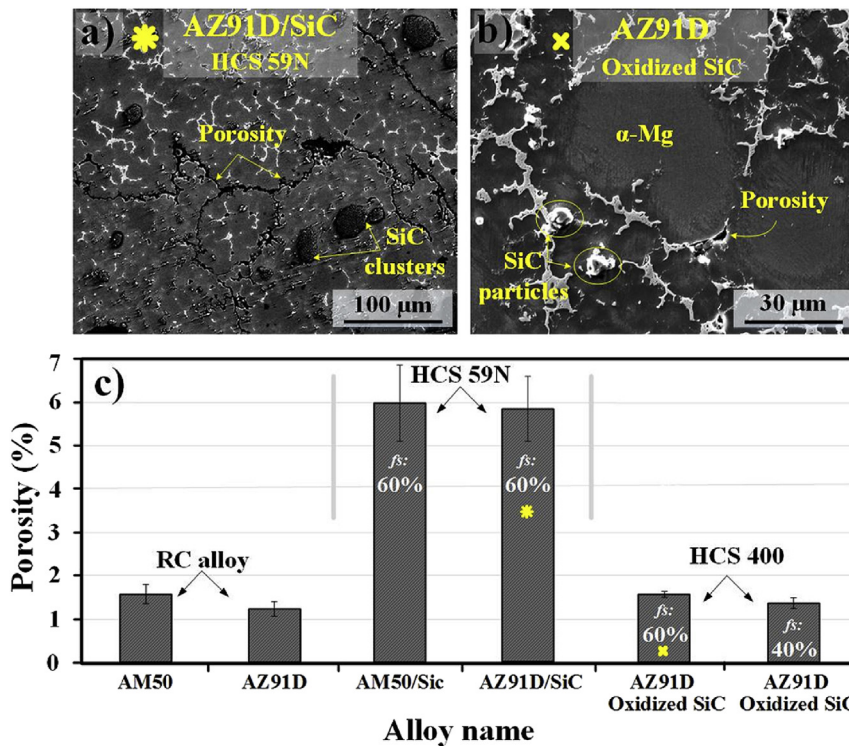


Fig. 11. Casting defects of the MMCs produced using the two different particle types and f_s values; (a) SEM micrograph showing the occurrence of connected porosities in the microstructure of alloy AZ91 reinforced by the SiC particle type HCS 59N, (b) the same alloy produced by the oxidized SiC particle type HCS 400 and (c) area fraction of porosity of all of the alloys and MMCs produced in this study. Please note the bars of Fig. 11c that correspond to the SEM images shown in Fig. 11a and b.

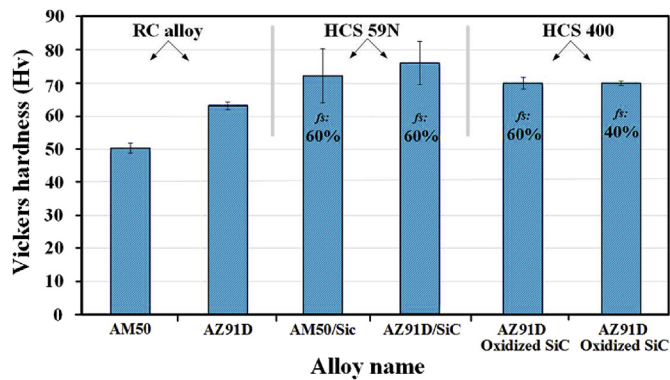


Fig. 12. Hardness of RC alloys and the MMCs produced by the two SiC particle types and f_s values.

includes micro- and macro-pores. It was obvious that the casting porosity was much less in the MMC produced HCS 400 than HCS 59N, which is in line with microstructural observations described above. As seen, while the as-cast RC materials exhibited a pore fraction of 1–2%, the RC alloy materials reinforced by the particle type HCS 59N showed a ~3 times higher fraction of pores. The fraction of casting pores decreased to almost the same values as their host alloys for the alloys reinforced by the oxidized HCS 400. Besides, the fraction of pores in the MMCs reached its minimum value when f_s was 40%. Thus, the trend in the extent of pores in the MMCs was similar to the clustering tendency and the uniformity of SiC particles.

3.5. Hardness measurements

The variations in hardness of the alloys AM50, AZ91 and the MMCs are shown in Fig. 12. It was evident that the MMCs were harder than their host alloys. It should be mentioned that huge variation in the hardness values due to the presence of SiC clusters (especially in the case of MMCs produced by HCS 59N) were omitted from the data. The use of HCS 59N as reinforcements resulted in the maximum hardness, increasing the hardness from ~50 to 73 and 64 to 76 for alloy AM50 and AZ91D, respectively. HCS 400 gave rise to a lower hardness than HCS 59N but still higher than RC AM50 and AZ91D. Unlike the MMCs' quality, decreasing the f_s value did not result in a higher hardness but one may consider the decrease in the scattering of the hardness results in the MMCs produced by HCS 400 using an f_s value of 40% compared to the other MMCs.

4. Discussion

Based on the reasons presented in the Introduction, it is highly desirable to produce Mg-based MMC cast components with uniform reinforcement distribution and structural integrity. The RC method in combination with the RheoMetal process has already established itself as a promising casting technique enabling the production of high-quality and complex cast Mg alloys with enhanced service performances [22,27,28]. Thus, one expected to detect a relatively low fraction of casting pores, in the range of 1–2% of the total examined area, in the RC AM50 and AZ91D alloys (see Figs. 2 and 11). In the case of RC alloys, the pores are frequently associated with the melt solidified in the inter-dendritic regions; see Fig. 2a. The commonly observed macro-porosities corresponding to large gas pores in the size range 100–500 μm , which are often formed in Mg alloys produced by the conventional HPDC method process, are not formed in the RC Mg alloys. This is a result

of the fact that the RC process induces strong shearing forces on the slurry, causing the feed rate of the casting to increase, and thereby resulting relatively quick fill speeds at high pressure [22]. It is known that trapped gases and bubbles are formed during filling, while shrinkage defects occur when feed metal is not accessible to compensate for shrinkage as the metal solidifies [20–22]. Hence, less risk for trapped gas as well as shrinkage is expected in RC AM50, which is in accordance with the results obtained in this study. The low temperatures and high apparent viscosity of the semi-solid slurry also leads to less porosity in castings made using the RC technique.

Perhaps the most vital part of the MMC technology is the science of interface as interfacial reactions embodies many of the important aspects of MMCs properties. When discussing MMCs and interfacial reactions/properties, wetting characteristics of the ceramic particles becomes a crucial concept [1,2]. Here, wettability is the ability of the molten metal to spread on a particle surface, and symbolizes the extent of intimate contact between the melt and ceramic particles [1]. Unluckily, the wettability of ceramic particles in molten Mg and Al and accordingly their alloys is poor, i.e. particles exhibit wetting angles considerably higher than 90° [15]. During the last two decades, various methods have been suggested to mitigate the wetting of ceramic particles by liquid metal, such as increasing metal liquid temperature, pre-treatment of particles (used in the second experiment in this study), and coating ceramic particles [47,48].

4.1. The first experiment-non-oxidized HCS 59N SiC particles

It is, indeed, attractive to fabricate MMCs using nano-sized ceramic reinforcements as the addition of micron size ceramic particles, can reduce the ductility of the matrix although improves strength significantly [24]. Mg alloys reinforced by sub-micron sized ceramic particles are usually made through powder metallurgy, disintegrated melt deposition, friction stir processing and ultrasonic vibration; see for e.g. Refs. [49–51]. In this study we employed the RC process for fabricating Mg alloy AM50-and AZ91D-based MMCs using sub-micron sized SiC particle type HCS 59N. This part of the work was combined with various types of analytical techniques including TEM/EDX/EELS to shed light on the formation of all microstructural constituents that may form in SiC-reinforced Mg-based composites. As expected, non-oxidized SiC particles strongly tended to form clusters in the MMCs' microstructures. It was quite challenging for us to achieve uniform dispersion of such small particles through casting as agglomeration and clustering frequently occurred during solidification due to high viscosity and poor wettability, the factors that are known to play a role in the soundness of nano-sized SiC-reinforced composites [52–55]. It may be noted that 10 vol.% of SiC, which was the case of this investigation, is a significant value of volume fraction for producing composites using nano-sized particles. Deng et al. [56], who attempted to produce Mg alloy AZ91 Mg matrix composites using sub-micron size SiC particulates using stir casting, only used 0.5–5 vol.% ceramic particles. Even though they employed many fewer fractions of SiC particles, they reported considerable amounts of SiC clusters in their MMCs' microstructures.

Moreover, the MMCs fabricated by HCS 59N exhibited the maximum fraction of casting pores, both in the central and skin areas of castings. In addition to the pores associated with the melt solidifying in the inter-dendritic regions, SiC cluster-porosity association was also observed, see Fig. 10b. In a few cases, worm-like pores were seen in the MMCs' microstructure, see Fig. 11a. In addition to the factors mentioned above, it is suggested that pores were mainly associated with the enormously large surface-to-volume ratio of SiC particles in the first experiment. Moreover,

SiC particles in the first experiment were poorly degassed that can be attributed to their fresh (non-oxidized) surfaces. Casting pores in MMCs are normally generated from the solidification shrinkage, the entrapment of gases and hydrogen evolution [57–59]. The entrapment of gases depends essentially on the processing parameters [56]. The hydrogen production is mainly the result of the reactions between the absorbed H₂O and Mg melt. Some water vapor is usually absorbed on the surface of the added particles, even though the particles are pre-heated. Once entering the melt, the water vapor can react strongly with Mg, forming MgO and releasing H₂. This also explains the formation of MgH₂ at the SiC particle/alloy interface; see Fig. 8. It may be noted that the hydride phase, α -MgH₂, has not previously been reported in the microstructure of Mg-based MMCs.

In the case of Mg alloy AM50, it was rather surprising that very little knowledge is available regarding the production of alloy AM50 reinforced by SiC particles, even when other ceramic particles are included. The only published work on the microstructure of alloy AM50-based MMC is the work done by Regev et al. [23]. They could successfully produce cast micron-sized SiC particle (in the range 4–30 μ m) reinforced AM50 using a SSM process. However, they did not provide detailed information concerning probable intermetallic particles and carbides. An interesting observation was made when we noticed that the β phase intermetallic particles were only formed with a much smaller fraction compared to the RC AM50 (Fig. 5a and b). Instead, a phase containing Mg, Al, Si and C was formed in the inter-dendritic regions (Fig. 5a and b). Such interference of nano-sized SiC particles in the composition of β phase was also observed in the microstructure of alloy AZ91 reinforced by the same particle type. This indicates another difficulty in producing Mg alloys-based MMCs using nano-sized particles as both β phase particles and tiny SiC particles tend to settle in the inter-dendritic regions during solidification of Mg alloys-based MMCs.

In contrast to the composition of the β phase, the sub-micron sized SiC additions did not have an considerable effect on the composition of η phase intermetallic (Al_x(Mn, Fe)_y) particles in both alloys as they formed with approximately the same fraction as the RC alloys (compare the brightest particles in Figs. 2 and 5). This was also confirmed by image analysis techniques. However, the morphology of η phase particles was somewhat different when comparing the microstructure of the MMCs and their monolithic counterparts. While η phase formed as semi-spherical particles in the RC materials, they appeared mostly as rod-like morphology in the MMCs (see for example Fig. 5a).

In the Mg-based MMCs, eutectic phases also form during the solidification process. These eutectic phases are able to wet the SiC particles and heterogeneously nucleate on the SiC substrate. The imperfections in the SiC particles, such as stacking faults, dislocations, and pits or grooves can act as favorable sites for heterogeneous nucleation [60]. In some cases, SiC particles near to the center of α -Mg grains were observed; see point 4 in Fig. 5 and Table 4, which may suggest that they were nucleation sites for the grains. The potency of SiC particles acting as nucleation sites in Mg-based alloys are discussed in Refs. [60,61]. Carbides were profoundly formed in the MMCs produced in the first experiment. It has been reported by several studies that carbides also play a role as grain refinements in the microstructure of Mg-based MMCs [62–65]. For example, Lu et al. [63], who examined the microstructure of an Mg-3%Al alloy reinforced by SiC particles, discussed the active role of the carbide Al₄C₃ in refining the grain structure of the MMC. Microstructural inspections (see for example Fig. 10a) showed the formation of small α -Mg grains due to the large population of active nucleation sites provided by the sub-micron sized SiC particles and carbides. Such microstructural configuration (with

a reduced average grain size) might be beneficial from a mechanical properties standpoint, according to the Hall–Petch equation [2,3], but may be detrimental from a corrosion standpoint. This stems from the fact that environmental degradation is an actual limiting factor for Mg-based alloys and that the atmospheric corrosion of Mg-based alloys is governed by the number of active cathodic sites and also available anodic sites [27–29].

SEM/EDX, XRD and TEM/EDX/EELS revealed the formation of MgO, Mg₂Si, MgH₂, Al₄C₃, Al₂MgC₂ as the reaction products of SiC particles and the melts. A possible mechanism for the formation of the hydride phase was provided above. The presence of MgO and Mg₂Si in the case of the alloys reinforced by non-oxidized particles was expected as the interaction of SiC particles with molten Mg that results in the formation of a mixture of Mg₂Si and MgO intermetallic particles. The carbides are commonly seen in the Mg-based MMCs and are said (see for e.g. Ref. [15]) to form based on the following reactions;



Generally, microstructural examination revealed fewer types of intermetallics and carbides when using the oxidized SiC particle type HCS 400 than when using HCS 59N as a result of the particles' stability provided by SiO₂. This can also partially explain the slightly lower hardness values of the MMCs produced in the second experiment than those produced in the first one.

4.2. The second experiment; oxidized HCS 400 SiC particles

In general, the MMCs produced by oxidized SiC particles (HCS 400) showed much better material quality. Thus, these MMCs produced through the RC technique exhibited a lower fraction of casting pores. The tendency for clustering and casting defects including the particle-associated pores and shrinkages was much less when oxidized HCS 400 using an f_s of 60% compared to that of HCS 59N and, interestingly, the difficulties associated with particle distribution and homogeneity were minimized, or almost eliminated, when the f_s decreased to 40%; see the SEM images in Fig. 6c and d and the quantitative assessments in Figs. 9 and 11. Thus, increasing the f_s during the RC process did not give rise to a better wetting of SiC particles, and accordingly more dispersion on ceramic particles. This is rather surprising as one could have expected to obtain an opposite effect of f_s on the quality of the MMCs as more mechanical stirring (by EEM), and accordingly better wetting of particles, should occur at higher f_s values. However, such increase in mechanical contacts between the EEM and the melts seems to have a negative effect on quality of Mg-based MMCs. Nevertheless, the fraction of casting pores was slightly lower in the MMCs when the f_s was 40% (see Fig. 11). To find out the reason behind the effect of solid fraction on the MMCs' quality future studies are planned by our research group. The presence of Mg₂C₃ carbides in the MMC produced by oxidized SiC particles was notable. The formation of Mg₂C₃ in the case of composites reinforced by the oxidized particles is most likely linked to the reaction of SiO₂ with molten Mg in some cases, and thus the melt became in contact with SiC particles to form carbides.

5. Conclusions

We produced Mg alloy AM50- and AZ91D-based MMCs using the rheoprocessing, whereby the slurry was produced by the RhoMetal process. The following conclusions can be drawn from this study:

1. TEM/EDX/EELS showed the presence of different intermetallic particles and Al carbides in the inter-dendritic regions of the MMC produced by non-oxidized fine (sub-micron sized) SiC particles. The hydride MgH₂, which was detected at the interface SiC/AZ91D, was suggested to be formed due to presence of water vapor on the surface of SiC particles, which resulted in the availability of H₂ in inter-dendritic regions during the solidification.
2. Oxidation (at 1100 °C for 45 min) of SiC particles resulted in less formation of undesired intermetallics and Al carbides in the microstructure of Mg alloys-based MMCs owing to the formation of SiO₂ on the SiC particles' surfaces.
3. The MMCs produced by macro-size oxidized particles exhibited low very low fraction of porosities, which was explained by desorption of adsorbed gases from SiC particle surfaces through the heat treatment procedure and significantly smaller number of specific surface areas as compared to the ones reinforced by nano-sized and non-oxidized SiC particles.
4. The quality of the MMCs was also examined using the NND and quadrat methods. It was shown that the slurry fraction has a great impact on the quality of the MMCs produced through the RC technique. Thus, the MMC produced by 40% of solid in their slurry exhibited much better dispersion of SiC particles as well as much fewer casting defects than that produced by 60% solid fraction. To understand the reason behind this effect, however, future studies are needed.

Altogether, it was shown that the rheocasting technique in combination with the RheoMetal process exhibits promising potential for fabricating Mg-based MMCs with very low fraction of casting defects as well as excellent homogeneity of macro-sized ceramic particles, if the right set of process parameters are employed. From the foundry point of view, the results of this study are of importance in order to optimize the process parameters further and to understand the RC process and thereby develop the technique for producing high quality Mg–Al casting alloys-based MMCs on an industrial scale.

Acknowledgment

The authors would like to express their deep thanks to the Swedish Foundation for Strategic Research (SSF) for funding this project.

References

- [1] Chawla N, Chawla KK. Metal matrix composites. New York: Springer Science Business Media; 2006.
- [2] Clyne TW, Withers PJ. An introduction to metal matrix composites. UK: Cambridge University Press; 1993.
- [3] Avedesian M, Baker H. Magnesium and magnesium alloys. ASM Materials Park; 1999.
- [4] Hassan SF, Gupta M. Development of high strength magnesium based composites using elemental nickel particulates as reinforcement. *J Mater Sci* 2007;37:2467–74.
- [5] Lu L, Thong KK, Gupta M. Mg-based composite reinforced by Mg₂Si. *Compos Sci Technol* 2003;63:627–32.
- [6] Zhang X, Zhang Q, Hu H. Tensile behaviour and microstructure of magnesium AM60-based hybrid composite containing Al₂O₃ fibres and particles. *Mater Sci Eng A* 2014;607:269–76.
- [7] Lu D, Jiang Y, Zhou R. Wear performance of nano-Al₂O₃ particles and CNTs reinforced magnesium matrix composites by friction stir processing. *Wear* 2013;305:286–90.
- [8] Paramsothy M, Tan XH, Chan J, Kwok R, Gupta M. Al₂O₃ nanoparticle addition to concentrated magnesium alloy AZ81: enhanced ductility. *J Alloy Comp* 2012;545:12–8.
- [9] Ferrel H, Mordike BL. Magnesium strengthened by SiC nanoparticles. *Mater Sci Eng A* 2001;298:193–9.
- [10] Gui M, Li P, Han J. Fabrication and characterization of cast magnesium matrix composites by vacuum stir casting process. *J Mater Eng Perform* 2003;12: 128–34.
- [11] Degischer HP, Schulz PA, Lacom W. Properties of continuous fibre reinforced Al and Mg-matrix composites produced by gas pressure infiltration. *Key Eng Mater* 1996;127–131:99–110.
- [12] Tun KS, Gupta M. Improving mechanical properties of magnesium using nano-yttria reinforcement and microwave assisted powder metallurgy method. *Compos Sci Technol* 2007;67:2657–64.
- [13] Liu YB, Lim SC, Lu L, Lai MO. Recent development in the fabrication of metal matrix-particulate composites using powder metallurgy techniques. *J Mater Sci* 1994;29:1999–2007.
- [14] Hu H. Squeeze casting of magnesium alloys and their composites. *J Mater Sci* 1998;33:1579–89.
- [15] Ye HZ, Liu XY. Review of recent studies in magnesium matrix composites. *J Mater Sci* 2004;39:6153–71.
- [16] Loh NH, Tor SB, Khor KA. Production of metal matrix composite part by powder injection molding. *J Mater Proc Technol* 2001;108:398–407.
- [17] Wang HY, Jiang QC, Li XL, Wang JG. In situ synthesis of TiC/Mg composites in molten magnesium. *Scr Mater* 2003;48:1349–54.
- [18] Siedersleben M. Vakuump-Druckguss von Magnesiumlegierungen für hochbelastete Bauteile, Magnesium Eigenschaften. Weinheim: Wiley-VCH; 2000.
- [19] Emley EF. Principals of magnesium technology. Oxford: Pergamon Press; 1966.
- [20] Ostklint M, Wessén M, Jarfors AEW. Microstructure and material soundness in liquid and rheocast AM50 and effect of section thickness. *Int J Cast Metal Res* 2014;27:235–41.
- [21] Ostklint M, Wessén M, Jarfors AEW. Microstructure and material soundness in liquid and rheocast AZ91: effect of section thickness. *Int J Cast Metal Res* 2015;28:65–71.
- [22] Esmaily M, Shahabi-Navid M, Mortazavi N, Svensson JE, Halvarsson M, Wessén M, et al. Microstructural characterization of the Mg–Al alloy AM50 produced by a newly developed rheo-casting process. *Mater Charac* 2014;95: 20–64.
- [23] Regev M, Rosenson H, Koren Z. Microstructure study of particle reinforced AZ91D and AM50 magnesium alloy semisolid casting. *Mater Sci Technol* 2007;23:1485–91.
- [24] Kleiner S, Beffort O, Wahlen A, Uggowitzer PJ. Microstructure and mechanical properties of squeeze cast and semi-solid cast Mg–Al alloys. *J Light Metal* 2002;2:277–80.
- [25] Kaufmann H, Potzinger R, Uggowitzer PJ. The relationship between processing and properties of new rheocast AZ91 and AZ71 magnesium alloys. *Light Metal Age* 2001:56–61.
- [26] Poddar P, Mukherjee S, Sahoo KL. The microstructure and mechanical properties of sic reinforced magnesium based composites by rheocasting process. *J Mater Eng Perf* 2009;18:849–55.
- [27] Esmaily M, Mortazavi N, Shahabi-Navid M, Svensson JE, Halvarsson M, Nyborg L, et al. Effect of rheocasting on corrosion of AM50 Mg alloy. *J Electrochem Soc* 2015;162:C85–95.
- [28] Esmaily M, Mortazavi N, Svensson JE, Halvarsson M, Blücher DB, Jarfors AEW, et al. Atmospheric corrosion of mg alloy AZ91d fabricated by a semi-solid casting technique: the influence of microstructure. *J Electrochem Soc* 2015;162:C311–21.
- [29] Esmaily M, Ström M, Svensson JE, Halvarsson M, Johansson LG. Corrosion behavior of alloy AM50 in semisolid cast and high-pressure die cast states in cyclic conditions. *Corrosion* 2015;71:737–48.
- [30] Walton WH. Feret's statistical diameter as a measure of particle size. *Nature* 1948;330:329–30.
- [31] Pyrz R. Quantitative description of the microstructure of composites. Part I: morphology of unidirectional composite systems. *Compos Sci Technol* 1994;50:197–208.
- [32] Tzamtzis S, Barekar NS, Babu H, Patel J, Dhindaw BK, Fan Z. Processing of advanced Al/SiC particulate metal matrix composites under intensive shearing - a novel rheo-process. *Compos Part A Appl Sci Manuf* 2009;40: 144–51.
- [33] Rogers A. Statistical analysis of spatial dispersions: the quadrat method Pion, London. 1974.
- [34] Bankoti AKS, Mondal AK, Kumar S, Ray BC. Individual and combined additions of calcium and antimony on microstructure and mechanical properties of squeeze-cast AZ91D magnesium alloy. *Mater Sci Eng A* 2015;626:186–94.
- [35] Luo S, Chen Q, Zhao Z. Effects of processing parameters on the microstructure of ECAE-formed AZ91D magnesium alloy in the semi-solid state. *J Alloy Comp* 2009;477:602–7.
- [36] Esmaily M, Shahabi-Navid M, Svensson JE, Halvarsson M, Nyborg L, Cao Y, et al. Influence of temperature on the atmospheric corrosion of the Mg–Al alloy AM50. *Corros Sci* 2015;90:420–33.
- [37] Ma Y, Zhang J, Yang M, J. Research on microstructure and alloy phases of AM50 magnesium alloy. *J Alloy Comp* 2009;470:515–21.
- [38] Mathaudhu SN, Sillekens WH, Neelameggham NR, Hort N, editors. TMS Magnesium technology, Orlando, FL, USA; 2012.
- [39] Agarwala V, Dixit D. Fabrication of aluminium base composite by foundry technique. *Trans Jpn Inst Met* 1981;22:521–6.
- [40] Harris RCA. Oxidation of 6H-alpha silicon carbide platelets. *J Am Ceram Soc* 1975;58:7–9.
- [41] Fukuda H, Kondoh K, Umeda J, Fugetsu B. Fabrication of magnesium based composites reinforced with carbon nanotubes having superior mechanical properties. *Mater Chem Phys* 2011;127:451–8.

- [42] Feldhoff A, Pippel E, Woltersdorf J. Carbon-fibre reinforced magnesium alloys: nanostructure and chemistry of interlayers and their effect on mechanical properties. *J Micros* 1999;196:185–93.
- [43] Russell-Stevens M, Todd R, Papakyriacou M. Microstructural analysis of a carbon fiber reinforced AZ91D magnesium alloy composite. *Surf Interface Anal* 2005;37:336–42.
- [44] Chua BW, Lu L, Lai MO. Influence of SiC particles on mechanical properties of Mg based composite. *Compos Struct* 1999;47:595–601.
- [45] Jeon KJ, Moon HR, Ruminski AM, Jiang B, Kisielowski C, Bardhan R, et al. Air-stable magnesium nanocomposites provide rapid and high-capacity hydrogen storage without using heavy-metal catalysts. *Nat Mater* 2011;10:286–90.
- [46] Danaie M, Tao SX, Kalisvaart P, Mitlin D. Analysis of deformation twins and the partially dehydrogenated microstructure in nanocrystalline magnesium hydride (MgH₂) powder. *Acta Mater* 2010;58:3162–72.
- [47] Rohatgi PK, Asthana R, Das S. Solidification, structures, and properties of cast metal-ceramic particle composites. *Inter Metal Rev* 1986;31:115–39.
- [48] Hashim J, Looney L, Hashmi MSJ. The wettability of SiC particles by molten aluminium alloy. *J Mater Process Technol* 2001;119:324–8.
- [49] Faraji G, Dastani O, Akbari Mousavi AA. Effect of process parameters on microstructure and micro-hardness of AZ91/Al₂O₃ surface composite produced by FSP. *J Mater Eng Perform* 2011;20:1583–90.
- [50] Nguyen QB, Gupta M. Increasing significantly the failure strain and work of fracture of solidification processed AZ31B using nano-Al₂O₃ particulates. *J Alloy Comp* 2008;459:244–50.
- [51] Shen MJ, Wang XJ, Li CD, Zhang MF, Hu XS, Zheng MY, et al. Effect of bimodal size SiC particulates on microstructure and mechanical properties of AZ31B magnesium matrix composites. *Mater Des* 2013;52:1011–7.
- [52] Deng K, Shi J, Wang C, Wang X, Wu Y, Nie K, et al. Microstructure and strengthening mechanism of bimodal size particle reinforced magnesium matrix composite. *Compos Part A Appl Sci Manuf* 2012;43:1280–4.
- [53] Oh S, Cornie J, Russell K. Wetting of ceramic particulates with liquid aluminum alloys: part II. Study of wettability. *Metall Trans* 1989;20A:533–41.
- [54] Eustathopoulos N, Nicholas MG, Drevet B. *Wettability at high temperature*. Kidlington: Elsevier; 1999.
- [55] Bahraini M, Minghetti T, Zoellig M, Schubert J, Berroth K, Schelle C, et al. Activated pressureless infiltration of metal-matrix composites with graded activator content. *Compos Part A Appl Sci Manuf* 2009;40:1566–72.
- [56] Deng KK, Wu K, Wu YW, Nie KB, Zheng MY. Effect of submicron size SiC particulates on microstructure and mechanical properties of AZ91 magnesium matrix composites. *J Alloy Comp* 2010;504:542–7.
- [57] Bindumadhavan PN, Chia TK, Chandrasekaran M, Wah HK, Lam LN, Prabhakar O. Effect of particle-porosity clusters on tribological behavior of cast aluminium alloy A356–SiCp metal matrix composites. *Mater Sci Eng A* 2001;315:217–26.
- [58] Gupta M, Sharon NML. *Magnesium, magnesium alloys, and magnesium composites*. John Wiley & Sons Inc; 2011.
- [59] Lu L, Dahle AK, StJohn DH. Grain refinement efficiency and mechanism of aluminium carbide in Mg–Al alloys. *Scr Mater* 2005;53:517–22.
- [60] Günther R, Hartig C, Bormann R. Grain refinement of AZ31 by (SiC)P: theoretical calculation and experiment. *Acta Mater* 2006;54:5591–7.
- [61] Cai Y, Taplin D, Tan MJ, Zhou W. Nucleation phenomenon in sic particulate reinforced magnesium composite. *Scr Mater* 1999;41:967–71.
- [62] Kim YM, Yim CD, You BS. Grain refining mechanism in Mg–Al base alloys with carbon addition. *Scr Mater* 2007;57:691–4.
- [63] Lu L, Dahle AK, StJohn DH. Heterogeneous nucleation of Mg–Al alloys. *Scr Mater* 2006;54:2197–201.
- [64] Qian M, Cao P. Discussions on grain refinement of magnesium alloys by carbon inoculation. *Scr Mater* 2005;52:415–9.
- [65] Tamura Y, Kono N, Motegi T, Sato E. Grain refinement of cast Mg–Al alloys. *J Jpn Inst Light Metal* 1998;48:395–9.